Supplemental Material – Nonlinear Poisson effect governed by mechanical critical transition

Jordan L. Shivers,[1,2] Sadjad Arzash,[1,2] and F. C. MacKintosh[1,2,3]

[1]*Department of Chemical and Biomolecular Engineering, Rice University, Houston, TX 77005*

[2]*Center for Theoretical Biological Physics, Rice University, Houston, TX 77030*

[3]*Departments of Chemistry and Physics and Astronomy, Rice University, Houston, TX 77005*

I. Network generation

After generating each initial network structure as described below, we reduce the connectivity z to the desired value by randomly removing bonds and any resulting dangling ends.

Mikado networks [1, 2] are prepared by depositing fibers of length L with random locations and orientations into a 2D periodic square unit cell of side length W and adding freely hinging crosslinks at all fiber intersections. We use $L = 4$ and $W = 30$ and continue depositing fibers until the average coordination number, after the removal of dangling ends, is $z \approx 3.6$. This yields an average crosslink density of $L/\ell_c \approx 11$, where ℓ_c is the average distance between crosslinks. We impose a minimum segment length $\ell_{min} = W/1000$.

2D and 3D packing-derived networks are prepared as in prior work [3]. For 2D PD networks, we randomly place $N = W^2$ radially bidisperse disks with $r \in \{r_0, \phi r_0\}$ in a periodic square unit cell of side length W and incrementally increase r_0 from 0, allowing the system to relax at each step, until the packing becomes isostatic and develops a finite bulk modulus. We use $\phi = 1.4$ to avoid long-range crystalline order [4]. At this point, we generate a contact network between overlapping disks. For 3D PD networks, we follow the same procedure beginning with $N = W^3$ radially bidisperse spheres, also with $r \in \{r_0, \phi r_0\}$ and $\phi = 1.4$, in a periodic cubic unit cell of side length W. We use $W = 20$ in 3D and $W = 100$ in 2D. For sufficiently large systems, this yields a network with initial coordination number $z \approx 2d$ [5–7], in which d is the dimensionality.

We generate 3D Voronoi networks by randomly distributing N seed points in a periodic cubic unit cell of side length W, from which we generate a Voronoi diagram using the CGAL library [8]. We choose N so that the final network has roughly W^3 nodes, with $W = 15$. These have initial average coordination number $z = 4$.

Three-dimensional random geometric graph (RGG) models have been shown to capture the micromechanics of collagen and fiber networks [9]. Following Ref. [9], we generate RGGs of $N = W^3$ vertices in a

periodic box of side length W, where each pair of nodes is connected with probability $P_c \propto e^{-\ell/L}/\ell^2$, where ℓ is the distance between two vertices and $L = 1$ is the length scale of a typical bond. We impose a minimum bond length of $\ell_{min} = 0.5$. We generate RGG networks with $W = 20$ and initial average coordination number $z = 4$.

II. Midpoints

The amount of contraction induced by the onset of stiffening depends on the resistance of the network to lateral compression. Mikado and 2D PD networks with relatively high values of z exhibit less dramatic contraction upon transitioning to the stretching-dominated regime than those with lower z. This is a consequence of the fact that more dilute (lower z) networks have fewer highly connected regions within them and are thus less resistant to compression than more highly connected networks. To verify that this is the case, in Fig. S1, we consider the same Mikado structures as in Fig. 3, in which we have now added a midpoint hinge to each bond in order to allow the buckling of individual bonds with the same bending energy penalty as is used between adjacent bonds. While the location of the transition in strain is still controlled by connectivity, networks with midpoints contract more dramatically at the critical strain than those without midpoints (for fixed $\tilde{\kappa}$), with larger corresponding peaks in $\tilde{\nu}$. This is because the normal stress induced by transverse compression in networks with midpoints is strictly proportional to the bending rigidity κ, whereas in networks without midpoints there can be additional, stronger contributions ($\propto \mu$) from locally stiff regions at large compression levels.

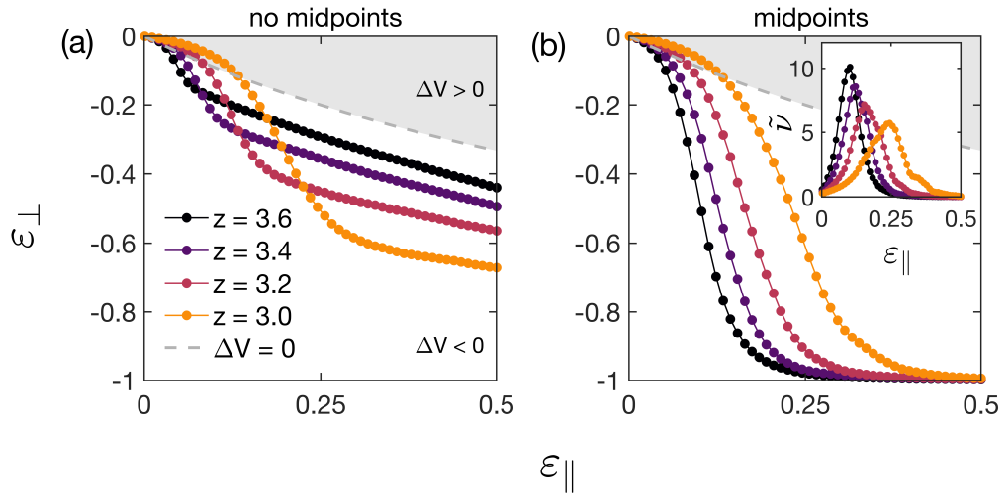

FIG. S1. Transverse strain $\varepsilon_\perp$ as a function of applied extensional strain $\varepsilon_\parallel$ for Mikado networks with $\tilde{\kappa} = 10^{-5}$ and varying connectivity z (a) without buckling of individual bonds and (b) with buckling of individual bonds, in which an extra node is added at the midpoint of each bond. The dashed line indicates the isochoric transverse strain, with the region above corresponding to an increase in volume ($\Delta V > 0$) and the region below corresponding to a decrease in volume ($\Delta V < 0$). Inset: Incremental Poisson's ratio $\tilde{\nu}$ as a function of $\varepsilon_\parallel$ for networks with midpoints. The corresponding plot for Mikado networks without midpoints is shown in Fig. 3a.

III. Energy contributions for networks with fixed z and varying $\tilde{\kappa}$

In Fig. S2, we plot the fractional contribution of bending to the total network energy, $\mathcal{H}_b/\mathcal{H}$, for a 2D packing-derived network with varying $\tilde{\kappa}$. In the low-$\tilde{\kappa}$ limit, we observe a clear transition from a bending-dominated to stretching-dominated regime at the critical strain, corresponding to the maximum value of the incremental Poisson's ratio $\tilde{\nu}$.

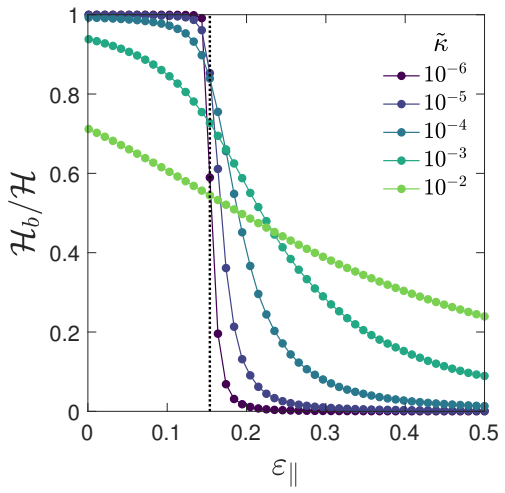

FIG. S2. Bending energy fraction $\mathcal{H}_b/\mathcal{H}$ for a 2D packing-derived network with $z = 3.2$, $W = 100$ and varying $\tilde{\kappa}$. The dotted line represents the critical strain $\varepsilon_{\parallel,c}$ corresponding to the peak in the incremental Poisson's ratio.

IV. Critical scaling

For subisostatic networks in the limit of small applied strain $\varepsilon_\parallel$, the differential Young's modulus $\tilde{E} = \partial\sigma_\parallel/\partial\varepsilon_\parallel$ is proportional to the bending rigidity $\tilde{\kappa}$. Above the critical applied strain $\varepsilon_{\parallel,c}$, $\tilde{E}$ is independent of $\tilde{\kappa}$ and scales as a power law with respect to the distance (along the strain axis) to the critical strain, i.e. $\tilde{E} \propto |\Delta\varepsilon_\parallel|^f$, where $\Delta\varepsilon_\parallel = \varepsilon_\parallel - \varepsilon_{\parallel,c}$. Following prior work [10], we can capture both regimes with the scaling form

$$\tilde{E}\frac{V}{V_0} \propto |\Delta\varepsilon_\parallel|^f \mathcal{G}_\pm\left(\frac{\tilde{\kappa}}{|\Delta\varepsilon_\parallel|^\phi}\right) \tag{1}$$

in which the scaling function $\mathcal{G}_\pm$ has branches corresponding to positive and negative values of $\Delta\varepsilon_\parallel$, and the factor V/V_0 corrects for the change in $\tilde{E}$ due to the change in the system's volume V from the initial volume V_0. In Fig. S3a, we show stiffening curves for a large packing-derived network with varying $\tilde{\kappa}$ and demonstrate scaling collapse according to the above scaling form with $f = 0.55$ and $\phi = 2.5$ (see Fig. S3b).

Recent work has described a hyperscaling relation between the stiffening exponent f, the dimensionality d, and the correlation length exponent ν, [11]

$$f = d\nu - 2, \tag{2}$$

and predicts that, at the critical strain, the differential nonaffinity should scale with system size W as

$$\max(\delta\Gamma) \propto W^{(\phi-f)/\nu}. \tag{3}$$

Determining ν from Eq. 2 using $d = 2$ and $f = 0.55$ (from the prior scaling collapse of $\tilde{E}$), we observe good

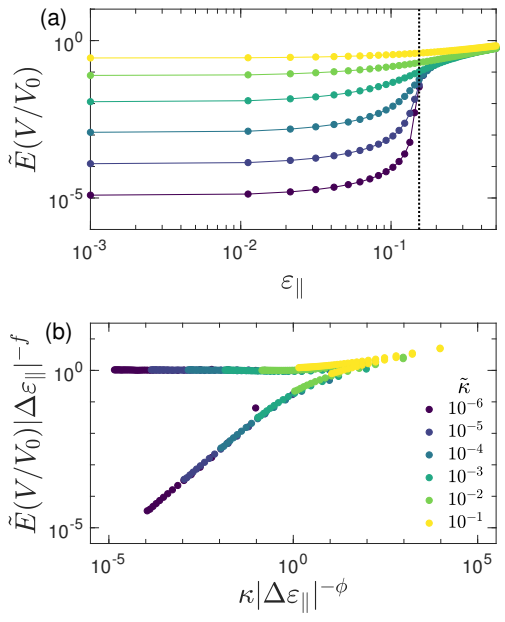

FIG. S3. (a) Stiffening curves for a 2D packing-derived network with varying κ, $z = 3.2$, $W = 140$. (b) Collapse of the curves in (a) according to Eq. 1 with exponents $f = 0.55$ and $\phi = 2.5$.

agreement between measured values of max($\delta\Gamma$) and the predicted scaling of the differential nonaffinity with system size (see Fig. S4).

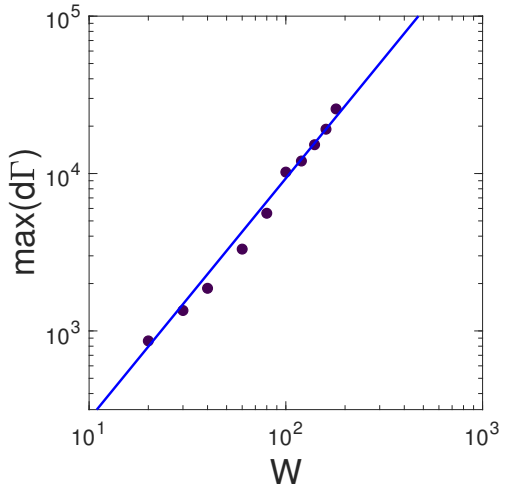

FIG. S4. In the low-$\tilde{\kappa}$ limit, the magnitude of the differential nonaffinity at the critical strain, max($\delta\Gamma$), grows with increasing system size W as max($\delta\Gamma$) $\propto W^{(\phi-f)/\nu}$ (solid line), with $f = 0.55$ and $\phi = 2.5$ obtained from the scaling collapse of the differential Young's modulus and $\nu = (f + 2)/d$ with dimensionality $d = 2$, as derived in Ref. [11]. These data correspond to averages over 2D packing-derived networks with $z = 3.2$ and $\tilde{\kappa} = 10^{-6}$.

V. Boundary conditions

Whereas we have exclusively considered periodic systems in this work to avoid boundary effects, we note that real systems are of course non-periodic. In experiments, strain is typically applied via fixed upper and lower boundaries, resulting in necking. Properly measuring transverse strain as a consequence of applied strain in experiments requires a sample with a sufficiently large aspect ratio (ratio of length along the applied strain axis to width along the transverse axes) to mitigate the influence of boundary effects. Prior experimental work [12] has addressed this issue by considering the strain within the necked region of a stretched cylindrical sample with a large aspect ratio. For a non-periodic simulated network with a sufficiently large aspect ratio, we expect that the strains in the center of the necked region should quantitatively agree with the corresponding strain in a sample with periodic boundary conditions (PBC). Smaller aspect ratios, however, are expected to reduce the apparent Poisson's ratio.

To test these assumptions, we generated periodic packing-derived according to the methods described in Section I above, with the initial network structure generated from $N = 10000$ radially bidisperse disks in a periodic box of aspect ratio α with initial dimensions $L_y = \alpha L_x$, where $L_x L_y = N$. After diluting the resulting network to $z = 3$, we cut all boundary-crossing bonds to yield a non-periodic network. We then designated the nodes on the top and bottom boundaries of the network as "fixed," and applied quasistatic strain to the sample by deforming the "fixed" nodes affinely according to the desired applied extension $\varepsilon_{\parallel}$ and minimizing the energy of the network at each applied strain. This results in a "necked" network configuration, as shown in Fig. S5, with the amount of apparent necking increasing with the aspect ratio. To obtain a coarse-grained estimate of the transverse strain within the necked region, we first bin the node coordinates according to their y-values into 100 equally spaced bins spanning the height of the network. We then measure the width of the network in each height bin as the difference between the maximum and minimum x-coordinates of the nodes within the bin. and measure the transverse strain $\varepsilon_{\perp} = w/w_0 - 1$ as the fractional change in the average width w of the middle 10% of bins (the center of the necked region) with respect to its initial value w_0. In Fig. S5c, we demonstrate that this effective transverse strain approaches that achieved with periodic boundary conditions as we increase the aspect ratio of the network sample. This indicates that "smearing out" of the phase transition due to necking does indeed occur if the aspect ratio of the sample is small, resulting in a smaller apparent Poisson's ratio (as shown in Fig. S5d), but that the results become equivalent when the aspect ratio is increased sufficiently (as in the experiments of Ref. [12]). We note that this results in a slight downward shift of the apparent critical strain, which can be understood as a result of the higher effective extensional strain near the center of a sample with fixed boundary conditions for a given global extensional strain.

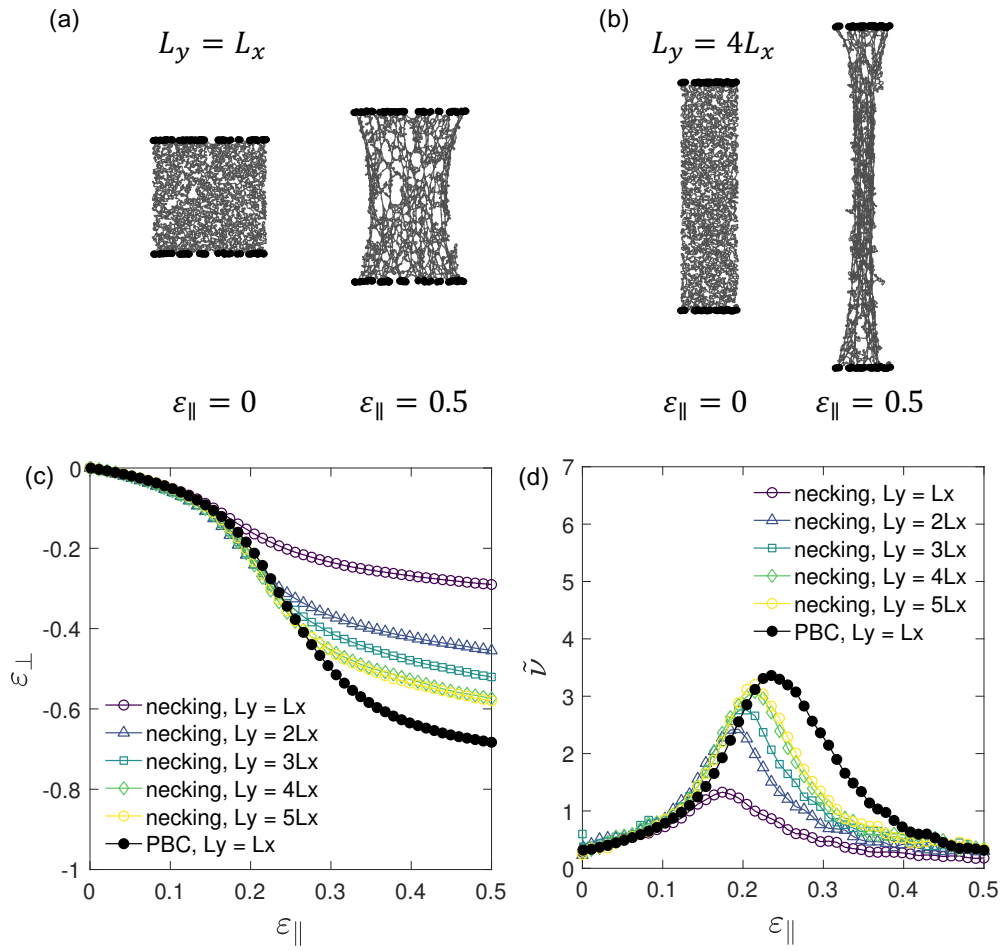

FIG. S5. (a-b) Non-periodic networks with fixed nodes (solid black circles) at the upper and lower boundaries exhibit necking under applied extensile strain. We consider networks with $\kappa = 10^{-4}$, generated from packings of $N = 10000$ bidisperse disks in periodic boxes of initial width L_x and height L_y, in which $L_x L_y = N$, with varying aspect ratio $\alpha = L_y/L_x$. These networks are then diluted to $z = 3$ and made non-periodic by cutting bonds that cross the boundaries. We affinely deform the "fixed" nodes by extensile strain ε, and the energy of the network is subsequently minimized with the positions of the "fixed" nodes held constant. The transverse strain $\varepsilon_\perp$ is measured as the change in width of the center of the network, as described above, as a function of applied extensile strain $\varepsilon_\parallel$. (c) We find that as the sample aspect ratio is increased, the $\varepsilon_\perp$ vs. $\varepsilon_\parallel$ curves for non-periodic samples approach the corresponding curve for a periodic networks with $L_x = L_y$. (d) Likewise, the incremental Poisson's ratio $\tilde{\nu} = -\partial\varepsilon_\perp/\partial\varepsilon_\parallel$ approaches that of the periodic samples. These data correspond to an average over 15 samples each.

VI. Excluded volume

We have thus far ignored excluded volume effects, as these are generally unimportant for networks of filamentous proteins such as collagen and fibrin due to the very low network volume fractions involved (typically less than 1%) and the suppressed bending fluctuations of such fibers. Especially for collagen

networks, models such as the present one have been shown to be quantitative and predictive, both in the linear regime and even far into the nonlinear regime.

To explore the influence of excluded volume effects on the nonlinear Poisson effect, we now consider simulations of 2D packing-derived networks with N_m equally spaced midpoint nodes on each bond, with and without including harmonic repulsive interactions between nodes (in this case, each node is treated as a repulsive disk with radius $r = 0.8/(2(N_m + 1))$ and repulsive spring constant $k_r = 1$, which is sufficiently large to prevent any bonds from interpenetrating at the strains we are considering). In Fig. S6a-b, we show images of sections of a network with $N_m = 5$ midpoints per bond.

In Fig. S6c, we show strain curves for networks of side length $L = 60$ with connectivity $z = 3.2$ and bending rigidity $\kappa = 10^{-5}$, in which we vary the number of midpoints per bond N_m between 1 and 5. For networks without repulsive interactions, the number of midpoints has essentially no effect on the strain curves (Fig S6c) or the corresponding incremental Poisson ratio (Fig S6d). When repulsive interactions are included, the excluded volume effect is significant for small N_m (i.e. large node radius and large effective bond thickness), but it becomes much less significant as N_m is increased. Further increasing N_m would result in the curves more closely resembling those of networks without repulsive interactions. For node radius r, we can approximate bonds as rods of width $2r$, so we can estimate an effective area fraction ϕ for a network with 2D line density ρ (bond length per area) and node radius r as $\phi = 2\rho r$. For connectivity $z = 3.2$, the 2D line density of our PD networks is $\rho \approx 1.4$, so we have an effective area fraction of $\phi \approx 0.18$ for $N_m = 5$ and $\phi \approx 0.56$ for $N_m = 1$. We note that these values are significantly larger than the volume fractions of experimentally tested networks ($\phi < 0.005$) [13, 14]. Since the effects of excluded volume in our 2D simulations are already quite small at the relatively large area fraction of $\phi = 0.18$, we conclude that simulations of networks without excluded volume effects are reasonable for this study.

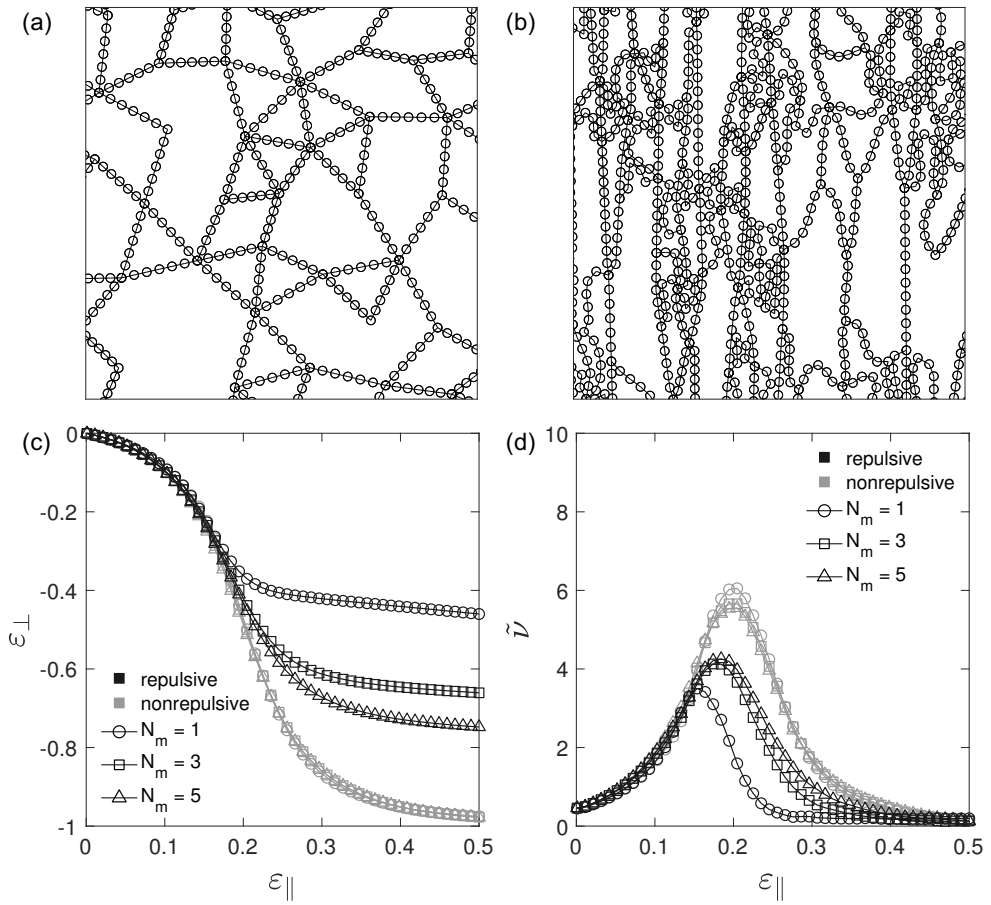

FIG. S6. Portions of a 2D packing-derived network with $\tilde{\kappa} = 10^{-5}$, $z = 3.2$, and $N_m = 5$ midpoints per bond with individual nodes acting as repulsive disks at (a) $\varepsilon_\parallel = 0$ and (b) $\varepsilon_\parallel = 0.3$. (c) Transverse strain $\varepsilon_\perp$ as a function of applied extensile strain $\varepsilon_\parallel$ for networks with $W = 60$, $z = 3.2$, and $\tilde{\kappa} = 10^{-5}$, in which the number of midpoints N_m is varied, with and without treating individual nodes as repulsive disks with radius $r = 0.8/(2(N_m + 1))$. (d) Incremental Poisson's ratio $\tilde{\nu} = -\partial\varepsilon_\perp/\partial\varepsilon_\parallel$ for the same networks.

VII. Growth of the critical strain with distance from isostaticity

In Fig. S7, we plot the critical strain $\varepsilon_{\parallel,c}$ as a function of the distance to the isostatic point, $z_c - z$, for 15 samples of 2D packing-derived networks with $W = 100$ and $\tilde{\kappa} = 10^{-5}$. Here we determined the critical strain $\varepsilon_{\parallel,c}$ for each sample as the inflection point of the stretching energy fraction $\mathcal{H}_s/\mathcal{H}$ when plotted as a function of $\varepsilon_\parallel$. We find that $\varepsilon_{\parallel,c} \propto (z_c - z)$ close to the isostatic point, in agreement with prior observations of the critical strain for packing-derived networks under shear strain [15]. This result may depend on the network structure and/or dilution protocol.

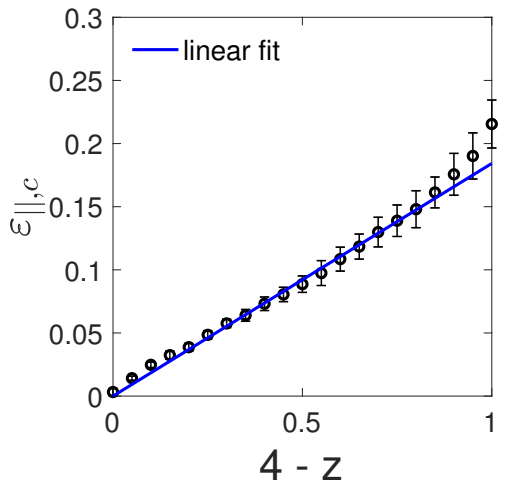

FIG. S7. The critical strain $\varepsilon_{\|,c}$ grows linearly with the distance to the isostatic point, $z_c - z$, for 2D packing-derived networks. These data correspond to 15 samples of 2D packing-derived networks with $W = 100$ and $\tilde{\kappa} = 10^{-5}$. Error bars are ± 1 standard deviation. The blue line corresponds to a linear fit of the 10 points closest to z_c.

VIII. Sample configurations

We have also included a zipped folder `config.zip` containing sample network configurations for each network type. A description of these files is available in the text file `config_readme.txt`.

[1] J. Wilhelm and E. Frey, Physical Review Letters **91**, 108103 (2003).

[2] D. A. Head, A. J. Levine, and F. C. MacKintosh, Physical Review Letters **91**, 108102 (2003).

[3] J. L. Shivers, J. Feng, A. Sharma, and F. C. MacKintosh, Soft Matter **15**, 1666 (2019).

[4] D. J. Koeze, D. Vågberg, B. B. Tjoa, and B. P. Tighe, Europhysics Letters **113**, 54001 (2016).

[5] M. Van Hecke, Journal of Physics Condensed Matter **22**, 033101 (2010).

[6] C. O'hern, L. Silbert, and S. Nagel, Physical Review E **68**, 11306 (2003).

[7] S. Dagois-Bohy, B. P. Tighe, J. Simon, S. Henkes, and M. Van Hecke, Physical Review Letters **109**, 095703 (2012).

[8] The CGAL Project, *CGAL User and Reference Manual*, 4th ed. (CGAL Editorial Board, 2013).

[9] F. Beroz, L. M. Jawerth, S. Münster, D. A. Weitz, C. P. Broedersz, and N. S. Wingreen, Nature Communications **8**, 16096 (2016).

[10] A. Sharma, A. J. Licup, K. A. Jansen, R. Rens, M. Sheinman, G. H. Koenderink, and F. C. MacKintosh, Nature Physics **12**, 584 (2016).

[11] J. L. Shivers, S. Arzash, A. Sharma, and F. C. MacKintosh, Physical Review Letters **122**, 188003 (2019).

[12] A. E. X. Brown, R. I. Litvinov, D. E. Discher, P. K. Purohit, and J. W. Weisel, Science **325**, 741 (2009).

[13] A. Sharma, A. J. Licup, R. Rens, M. Vahabi, K. A. Jansen, G. H. Koenderink, and F. C. MacKintosh, Physical Review E **94**, 042407 (2016).

[14] K. A. Jansen, A. J. Licup, A. Sharma, R. Rens, F. C. MacKintosh, and G. H. Koenderink, Biophysical Journal **114**, 2665 (2018).

[15] M. Wyart, H. Liang, A. Kabla, and L. Mahadevan, Physical Review Letters **101**, 215501 (2008).